ELSEVIER

Contents lists available at ScienceDirect

Earth and Planetary Science Letters

www.elsevier.com/locate/epsl



Crustal tilting and differential exhumation of Gangdese Batholith in southern Tibet revealed by bedrock pressures



Wenrong Cao ^{a,*}, Jiaming Yang ^a, Andrew V. Zuza ^b, Wei-Qiang Ji ^c, Xu-Xuan Ma ^d, Xu Chu ^e, Quentin P. Burgess ^a

- a Department of Geological Sciences and Engineering, University of Nevada, Reno, MS-172, 1664 N. Virginia St., Reno, NV 89557, United States of America
- b Nevada Bureau of Mines and Geology, University of Nevada, Reno, MS-178, 1664 N. Virginia St., Reno, NV 89557, United States of America
- c State Key Laboratory of Lithospheric Evolution, Institute of Geology and Geophysics, Chinese Academy of Sciences, P.O. Box 9825, Beijing 100029, China
- d Key Laboratory of Deep-Earth Dynamics of Ministry of Natural Resources, Institute of Geology, Chinese Academy of Geological Sciences, Beijing 100037, China
- e Department of Earth Sciences, University of Toronto, 22 Russell Street, Toronto, Ontario, M5S3B1, Canada

ARTICLE INFO

Article history: Received 11 March 2020 Received in revised form 9 May 2020 Accepted 14 May 2020 Available online xxxx Editor: A. Yin

Keywords:
Gangdese Batholith
southern Tibet
pluton emplacement depth
crustal tilting
exhumation

ABSTRACT

The exhumation history of the Gangdese Batholith, southern Tibet, bears on how magmatism and tectonism interact with surface processes in a long-lived magmatic orogen. In this study, we applied Alin-hornblende barometry across the eastern Gangdese Batholith to obtain pluton emplacement pressures. Our results, together with existing bedrock pressure data, reveal the regional paleo-depth pattern across the Gangdese Batholith. The western part of the batholith, near Lhasa, exposes plutons emplaced at 1-2 kbar whereas the eastern part, near Nyingchi, exposes crust recording pressures typically of 6-12 kbar. We coupled pressure data with new and published U-Pb zircon ages to constrain the exhumation history of the Gangdese Batholith. The results show that since 100 Ma, the upper crust experienced limited exhumation except a pronounced Oligocene-Miocene pulse. In contrast, the middle-lower crust experienced a complex exhumation and burial history, reflecting major tectonic events including the development of continental arc and continent-continent collision. Since ca. 10 Ma, the eastern Nyingchi sector experienced fast exhumation (total exhumation > 40 km), which was likely related to the exhumation of the Eastern Himalayan Syntaxis. The Lhasa sector experienced comparatively limited exhumation (total exhumation < 10 km), Such dramatic differential exhumation along the E-W direction requires that the Gangdese Batholith was tilted to present-day exposure levels. Our study shows that during the evolution of a magmatic orogen, the upper and middle-lower crust can behave differently, and the exhumation history reflects integrated tectonic, magmatic, and surface processes. The surface erosion rate estimates can be used to calculate CO2 consumption and evaluate the roles of magmatic orogens in the long-term carbon cycle. Given its great exposures of plutonic and metamorphic rocks across a relatively continuous crustal section, the Gangdese Batholith has great potential to serve as a natural laboratory to understand the structures and evolution of the continental crust.

© 2020 Elsevier B.V. All rights reserved.

1. Introduction

Tilted orogenic crustal sections are valuable geological windows to understand the vertical gradients of the composition and structures of the orogens (e.g., Ducea et al., 2015). Fundamental to establishing the framework in the vertical dimension is to quantitatively establish the bedrock pressure patterns (paleo-depths). The present-day bedrock pressure patterns also reflect the exhumation, burial, and tilting histories of the crust in response to tectonic and

magmatic events (Stüwe and Barr, 1998), as well as the surface processes which alter the geomorphology of metamorphism (Willett, 1999). The Gangdese Batholith in the southern Tibet is the magmatic product that developed in response to the northward subduction of the Neo-Tethyan plate beneath the Eurasian plate, and the subsequent India-Eurasia collision (e.g., Yin and Harrison, 2000; Kapp et al., 2007; Zhu et al., 2015; Zuza et al., 2018). Although significant research has focused on the composition and temporal history of the batholith (e.g., Ji et al., 2014; Zhu et al., 2015), the regional bedrock pressure pattern is poorly constrained compared to other well-studied magmatic crustal sections such as the Sierra Nevada Arc in California (Chapman et al., 2012) and the Kohistan Arc in Pakistan (Jagoutz, 2014). Furthermore, existing

^{*} Corresponding author.

E-mail addresses: caowenrong@gmail.com, wenrongc@unr.edu (W. Cao).

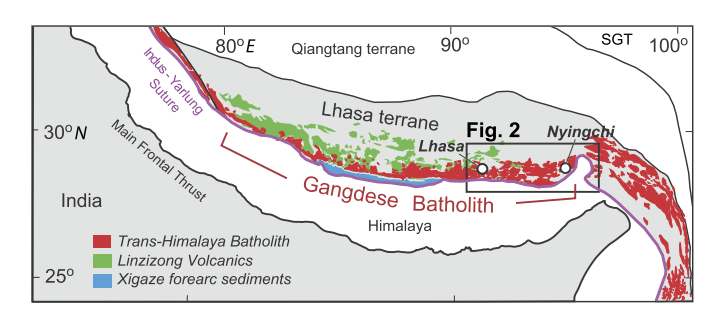


Fig. 1. Simplified geologic map of southern Tibetan plateau showing major tectonic regimes. The Gangdese Batholith is the central section of the Tans-Himalaya Batholith developed along the southern edge of the Lhasa terrane. SGT: Songpan-Ganze terrane. Modified from Ji et al. (2014). (For interpretation of the colors in the figure(s), the reader is referred to the web version of this article.)

exhumation/cooling data from the Gangdese Batholith is confined mostly to the Oligocene-Miocene-to-present timeframe (e.g., Harrison et al., 2000; Tremblay et al., 2015). Little is known about the exhumation of the Gangdese Batholith from the Cretaceous to Paleocene and how rocks of different depths exhume over a ~ 100 Myr timescale. Finally, there is a recent focus on the role of magmatic orogens as CO2 sources due to magmatic and metamorphic degassing (e.g., Lee et al., 2013), but the role of the magmatic orogens as CO2 sinks due to silicate weathering (Jiang and Lee, 2019) is less well established. One of the reasons hampering the CO₂ consumption calculation is that the estimation of the flux of silicate weathering requires a robust understanding of surface erosion rates over geologic timescales, which are poorly resolved for many magmatic orogens including the Gangdese. To address the above challenges, we integrated newly obtained pluton emplacement pressure data with published bedrock pressures to reveal the regional paleo-depth pattern across the Gangdese Batholith and constructed an exhumation history of the Gangdese Batholith that extends back to the Late Cretaceous.

2. Gangdese Batholith

The \sim 1500-km-long Gangdese Batholith in southern Tibet is the central segment of the granitoid belts of "Trans-Himalayan Batholith" along the southern margin of the Eurasian plate (Fig. 1). Mesozoic-early Cenozoic subduction of the Neo-Tethyan plate accommodated the convergence between the Indian and Eurasian plates until their collision at ca. 60-55 Ma (e.g., Yin and Harrison, 2000; DeCelles et al., 2014). This collision is marked by the Indus-

Yarlung suture zone (IYSZ), and intrusions related to the subduction and collision are distributed across the batholith largely to the north of the suture (Zhu et al., 2015). Magmatism of the Gangdese Batholith spans from Middle-Late Triassic to late Miocene, and U/Pb zircon ages display temporal peaks (High-Flux Events, HFE, or flare-ups) around 90-100 Ma, 50-60 Ma, and 10-20 Ma (Chapman and Kapp, 2017; Ji et al., 2014; Zhu et al., 2015). The 90-100 Ma peak is associated with continental arc magmatism, and the 50-60 Ma peak is attributed to the breakoff of the subducted Neo-Tethyan plate after the initial collision (e.g., Zhu et al., 2015) or arc root foundering (Kapp et al., 2007). The 10-20 Ma peak may represent delamination of the Asian mantle and crustal extension (e.g., (Chung et al., 2009)).

3. Geology of study area

The study area is a \sim 400-km-long, \sim 40-km-wide E-W corridor from west of Lhasa (90°E) to east of Nyingchi (95°E) (Fig. 2). Existing U-Pb zircon ages from the study are show peaks at ca. 90 Ma, 50 Ma, and 15 Ma mimicking the age pattern of the entire Gangdese Batholith (Fig. 3A).

The stratigraphy of the study area includes the following units, in order from oldest to youngest respectively: (1) reworked mid-Proterozoic and Cambrian crystalline basement, separated with Paleozoic-Triassic marine clastic rocks and limestone by fault contacts (Yin et al., 1988); (2) Triassic-Jurassic volcanics, Upper Jurassic-Lower Cretaceous fluvial, and marginal marine sandstone, shale, and flysch, mid-Cretaceous shallow marine limestone, and Upper Cretaceous fluvial red beds (e.g., Yin et al., 1988); (3) Paleocene-Eocene volcanics of the Linzizong Formation, made up of \sim 3500 m of volcanic strata of andesitic lava, dacitic to rhyolitic tuffs that have been dated between 69-50 Ma (He et al., 2007; Zhu et al., 2015); and (4) locally exposed Miocene sandstone and conglomerate related to the development of regional thrust faults (Yin et al., 1994) and extensional basins (DeCelles et al., 2011).

The exposure level of crustal rocks deepens from west to east as evidenced by an increase in metamorphic grade (Fig. 4A). Supracrustal rocks, including the Linzizong volcanics, upper Mesozoic sedimentary strata, and porphyritic plutons, are exposed around Lhasa (90.5-92°E) (Fig. 5A, B). These volcanic-sedimentary rocks are weakly to non-metamorphosed. Greenschist facies slateyphyllitic foliation are commonly found in the Mesozoic strata. In contrast, rocks of middle-lower crustal levels are exposed in the east near Nyingchi (93.5-95°E). These rocks include plutons containing magmatic epidote that record intense magmatic-ductile

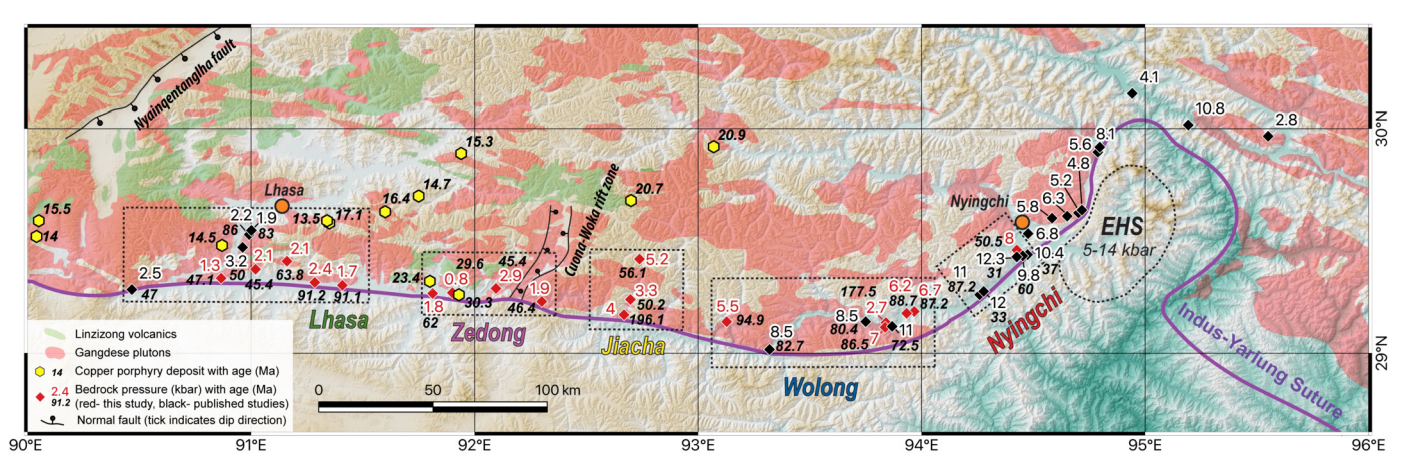


Fig. 2. Map of Lhasa-Nyingchi area. Gangdese Batholith and Linzizong volcanics are highlighted using red and green colors. Bedrock pressure data and copper porphyry deposits are shown with associated ages. Bedrock pressure data in the study area are binned into five sectors (Lhasa, Zedong, Jiacha, Wolong, Nyingchi) shown as boxes with dashed outlines. EHS: Eastern Himalayan Syntaxis. Map based on 1:1.5 million metamorphic geological map of the Tibetan Plateau and its surrounding areas. National Tibetan Plateau Data Center.

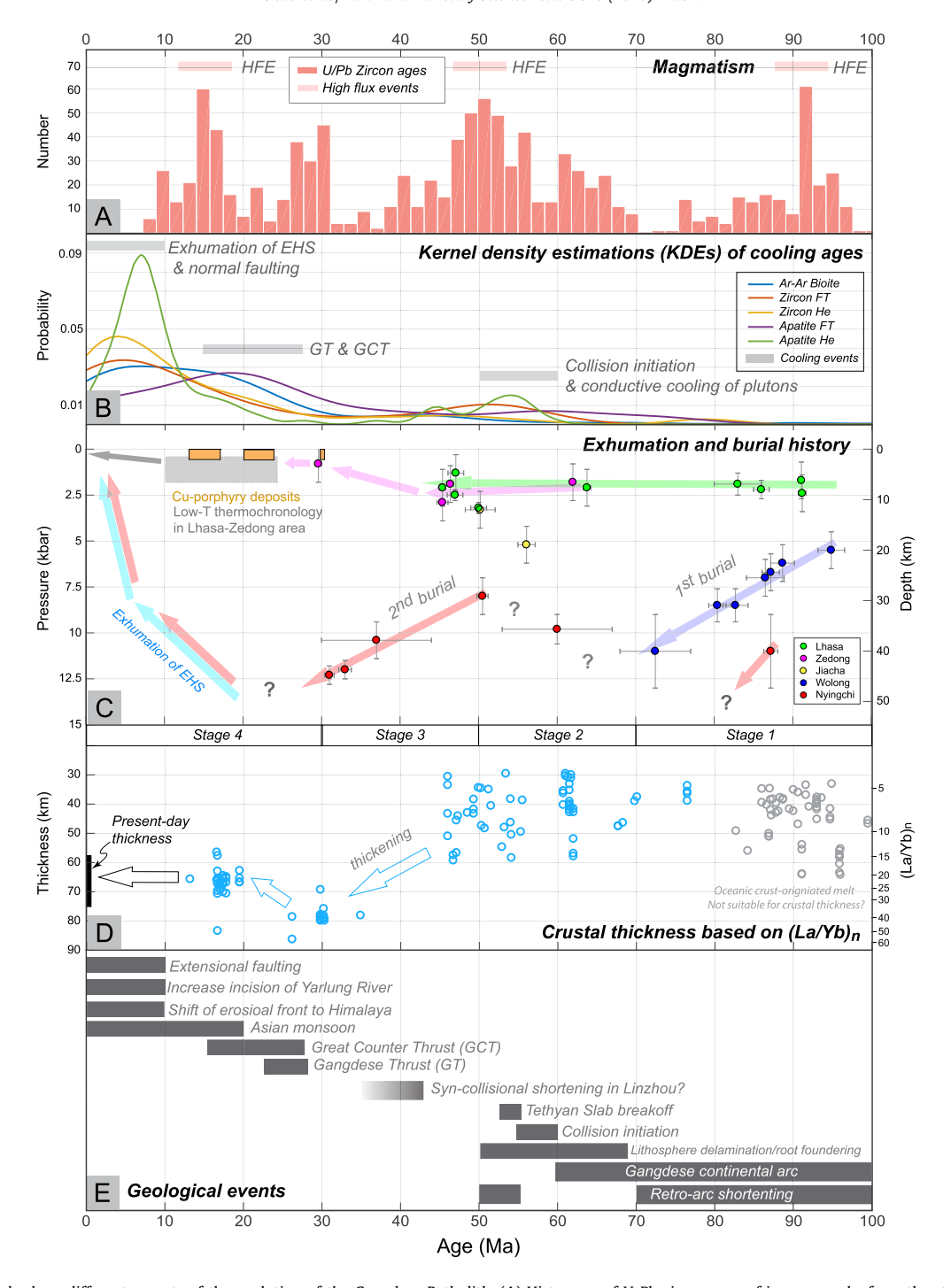


Fig. 3. Multiple panels show different aspects of the evolution of the Gangdese Batholith. (A) Histogram of U-Pb zircon ages of igneous rocks from the study area. Horizontal bars show the regional High-Flux Event (HFE, or magmatic flare-ups) at 93 Ma, 50 Ma, and 15 Ma. Age data are from Chapman and Kapp (2017)'s Tibetan Magmatism Database. (B) Kernel density estimations (KDEs) of cooling ages including Ar/Ar Biotite ages, zircon and apatite fission-track, (U-Th)He ages. The compiled dataset can be found in the Supplementary Materials. Grey bars show major cooling events suggested by the overlapping of the KDEs. The KDEs are generated using MATLAB fitdist function with the default bandwidth. (C) Exhumation/burial paths constructed based on bedrock pressure data. Colors of the paths correspond to five sectors. (D) Crustal thickness estimates in study area based on whole-rock (La/Yb)_n ratio (Zhu et al., 2017). Present-day crustal thickness is based on CRUST 1.0 model (Laske et al., 2013). (E) Regional geological events affected the Gangdese Batholith. GT: Gangdese Thrust. GCT: Great Counter Thrust. EHS: Eastern Himalayan Syntaxis.

deformation, and migmatitic gneiss (Fig. 5C, D). To the east of Nyingchi, and to the south of the Indus-Yarlung suture zone, the Eastern Himalayan Syntaxis (EHS) represents an exhumed highly-strained lower crust of typical pressures of 5-14 kbar (e.g., Ding et al., 2001; Booth et al., 2009).

Most previous research of the exhumation history of Gangdese Batholith in southern Tibet tracked the Oligocene-Miocene cooling history via medium to low-temperature thermochronology, including multi-diffusion domain (MDD) modeling of K-feldspar, biotite and hornblende ⁴⁰Ar/³⁹Ar ages, and (U-Th)/He and fission track dating of apatite and zircon (e.g., Harrison et al., 2000; Dai et al., 2013; Tremblay et al., 2015) (Fig. 3B). Three cooling events have been interpreted to reflect the initial continental collision (e.g., Dai et al., 2013) and conductive cooling of Gangdese plutons around 55 Ma, activation of Gangdese Thrust and Great Counter Thrust during 28-15 Ma (e.g., Harrison et al., 2000; Laskowski et al., 2018),

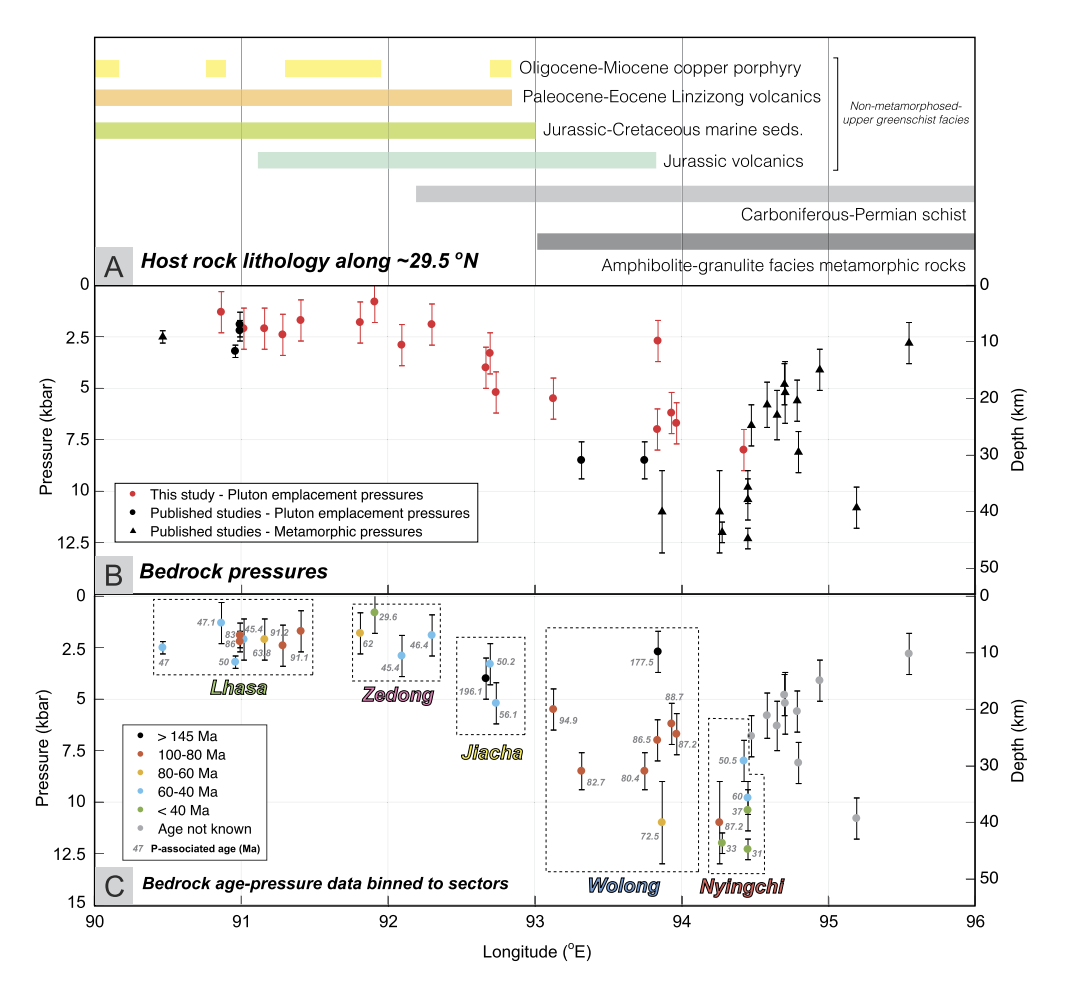


Fig. 4. (A) Host rock lithology along 29.5° N latitude. (B) Bedrock pressures to the north of the Indus-Yarlung Suture. Error bar presents the standard deviation. (C) Bedrock pressures with pressure-associated ages. 1 kbar = 3.64 km conversion is used based on the density of crustal rock of 2800 kg/m^3 and gravitational acceleration of 9.8 m/s^2 .

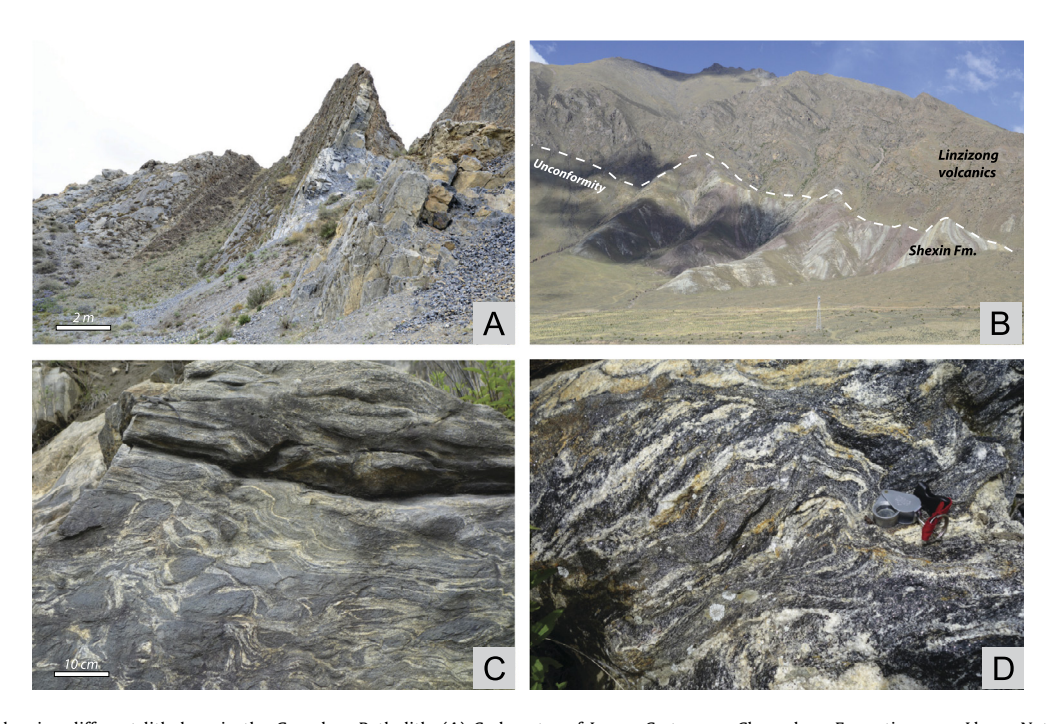


Fig. 5. Field photos showing different lithology in the Gangdese Batholith. (A) Carbonates of Lower Cretaceous Chumulong Formation near Lhasa. Note the beds have been tilted but rocks are not metamorphosed. (B) Angular unconformity between underlying folded Upper Cretaceous Shexing Formation (clastic sediments) and overlying massive Eocene Linzizong volcanics. Photo taken near Maxiang (40 km to NW of Lhasa). (C) Middle-lower crust magma mingling and complex deformation near Nyingchi. (D) Migmatitic gneiss near Nyingchi.

Table 1Locations, ages, emplacement pressures, and solidus temperatures of barometry samples.

Sample	Lat.	Long.	Elev. (m)	Lithology	Sector	Age (Ma)	P (kbar) A&S ¹	P (kbar) Mutch ²	P (kbar) Mean	± ³	Temp (°C) ⁴	Age reference ⁵
7-6-1*	29.45952	94.42608	2930	Monzodiorite	Nyingchi	50.5 ± 0.7	8.1	7.8	8.0	1.0	726	This study
7-13 [*]	29.1855	93.96752	2980	Granodiorite	Wolong	87.2 ± 1.1	(6.8)	6.5	6.7	1.0	736	Ji et al. (2014)
7-14	29.17734	93.93331	2997	Granodiorite	Wolong	88.7 ± 1.5	(5.5)	6.8	6.2	1.0	797	Ma et al. (2013)
XCT55	29.1360	93.8409	3340	Granite	Wolong	177.5 ± 1.1	3.0	2.5	2.7	1.0	655	This study
ML04-1*	29.12564	93.8370	2960	Monzodiorite	Wolong	86.5 ± 2.4	7.5	6.5	7.0	1.0	704	Ji et al. (2014)
09FW34*	29.14	93.1283	3100	Tonalite	Wolong	94.9 ± 1.7	6.0	5.0	5.5	1.0	699	Ji et al. (2014)
09FW41	29.4193	92.7381	4520	Granite	Jiacha	56.1 ± 1.1	6.0	4.5	5.2	1.0	661	Ji et al. (2012)
09FW50*	29.2388	92.6973	3780	Granodiorite	Jiacha	50.2 ± 1.9	(3.7)	2.9	3.3	1.0	665	Ji et al. (2012)
XCT56	29.1708	92.6687	3420	Granite	Jiacha	196.1 ± 1.2	(4.5)	3.5	4.0	1.0	669	This study
XCT58	29.2301	92.3008	3590	Granite	Zedong	46.4 ± 0.4	(1.8)	1.9	1.9	1.0	667	This study
8-4	29.28817	92.09571	3561	Monzodiorite	Zedong	45.4 ± 0.7	3.1	2.7	2.9	1.0	695	Ji et al. (2012)
8-6	29.26903	91.9114	3553	Monzodiorite	Zedong	29.6 ± 0.4	(0.4)	1.2	0.8	1.0	629	Zhang et al. (2014)
8-10	29.26566	91.81249	3558	Granodiorite	Zedong	62	(1.4)	2.1	1.8	1.0	745	Jiang et al. (2014)
10-7-1	29.30214	91.40829	3558	Monzodiorite	Lhasa	91.1	(1.7)	1.8	1.7	1.0	633	Jiang et al. (2014)
10-8	29.31496	91.28507	3578	Monzodiorite	Lhasa	91.2 ± 0.5	(2.4)	2.3	2.4	1.0	702	This study
11-10	29.4094	91.16078	3770	Granodiorite	Lhasa	63.8 ± 0.5	(2.0)	2.1	2.1	1.0	712	This study
12-14	29.37394	91.01984	3756	Qtz Monzodiorite	Lhasa	45.4 ± 0.4	(2.1)	2.0	2.1	1.0	683	This study
14-7	29.33386	90.86615	3580	Granodiorite	Lhasa	47.1 ± 1.0	(1.3)	1.2	1.3	1.0	662	Ji et al. (2009)

¹ Pressure results based on Anderson and Smith (1995)'s calibration with temperature effect corrected. Pressures in paracenteses are the results having Fe[#] < 0.4 or Fe³⁺/(Fe³⁺ + Fe²⁺) < 0.2. These pressures are still considered to be valid since they pass the Fe[#] > 0.65 and T < 800 °C filters (Putirka, 2016).

- ² Pressure results based on Mutch et al. (2016)'s calibration.
- ³ A standard error of 1 kbar is assumed.
- ⁴ Solidus temperature obtained from plagioclase thermometer (Holland and Blundy, 1994).
- ⁵ Information from Tibetan Magmatism Database (Chapman and Kapp, 2017).
- * Mark in the sample column suggests sample containing magmatic epidote.

and exhumation of the Eastern Himalayan Syntaxis and normal faulting since ca. 10 Ma (e.g., Ding et al., 2001; Zeitler et al., 2014; Kapp et al., 2005). Little is known about any earlier Cretaceous to Eocene exhumation. The amount of the exhumation constrained by medium to low-T thermochronology is also typically limited to <10 km due to the lower closure temperatures of the thermochronometers (<200-400 °C) and is subjected to the uncertainty of varying geothermal gradients (e.g., Reiners and Brandon, 2006).

Another useful regional marker of exhumation is the Oligocene-Middle Miocene copper-porphyry deposits that are scattered along the southern margin of the Lhasa terrane from 88°E to 93°E (Yang et al., 2016) (Fig. 2, Fig. 4A). Copper-porphyry deposits are known to form at a shallow depth (1-5 km with average 2 km) (Yanites and Kesler, 2015) and therefore their exposure at the surface requires limited exhumation <5 km. The preservation of the Linzizong Formation also suggests that the overall limited exhumation of the upper crust to the west of 93°E since 69-50 Ma (Fig. 2, Fig. 4A).

4. Approach

To obtain estimates of the paleo-depth of the Gangdese Batholith, we collected granitoid samples for Al-in-hornblende barometry along the highway from Lhasa to Nyingchi, immediately north of the Indus-Yarlung suture (Fig. 2, Table 1). We used the Tibetan Magmatism Database (Chapman and Kapp, 2017) as a guide. Samples for U-Pb zircon geochronology were also collected from plutons of unknown age. The elevation difference among the samples is less than 2 km (minimum 2930 m, maximum 4520 m). We also compiled existing bedrock pressures from the literature (Fig. 2, Fig. 4B). Metamorphic pressures were obtained from mineral assemblages and metamorphic barometers. Ages associated with the metamorphic pressures were constrained from metamorphic monazite and overgrowth rim of zircon. Existing pluton emplacement pressures have also been compiled into the database. The compiled bedrock pressure data can be found in the Supplementary Materials.

Exhumation or burial of a block of crust can be obtained by calculating the pressure difference between adjacent bedrocks of different ages. Exhumation/burial rate is calculated by dividing the pressure difference by the difference of ages associated with the pressures (Fig. 6A). This approach assumes that the relative position of the existing plutons or metamorphic host rocks remains unchanged although they could move vertically together during a younger exhumation or burial event. We will further justify this approach using Gangdese geology in Section 7.3.1. Ideally, these pressure-age data should be from one locality. Due to the spatial distribution of available pressure-age data, the pressure-age data was binned into five 50-100 km-sized orogen-parallel sectors: from west to east, Lhasa, Zedong, Jiacha, Wolong, and Nyingchi (Fig. 2). We argue that at the 10³ km orogen-parallel scale, regional exhumation patterns should be approximately consistent for a region of 10¹-10² km. In other words, within a sector of 50-100 km size, the crust exhumes similarly. Examples of consistent exhumation patterns across regions of 10¹-10² km size include the Eastern Himalayan Syntaxis (Zeitler et al., 2014) and the southern Sierra Nevada (Chapman et al., 2012). Compared to the medium to lowtemperature thermochronology, using bedrock pressures to track exhumation has the following advantages: (1) emplacement pressure is difficult to be reset; (2) U-Pb zircon age associated with the emplacement pressure is unambiguous; (3) pressure can be directly translated to depth, and no assumption of geothermal gradient is needed; and (4) the broad range of crystallization ages of Gangdese plutons allows for tracking the exhumation back to Late Cretaceous.

5. Analytical methods

5.1. Al-in-hornblende barometry

The Al-in-hornblende (Al-in-Hbl) barometry has been widely used to constrain the emplacement pressure of calc-alkaline, felsic-intermediate plutons typical for arcs (e.g., Hammarstrom and Zen, 1986; Ague and Brandon, 1992; Jagoutz, 2014). The requisite mineral assemblage is needed to ensure the barometry work properly (e.g., Anderson and Smith, 1995). The mineral assemblage

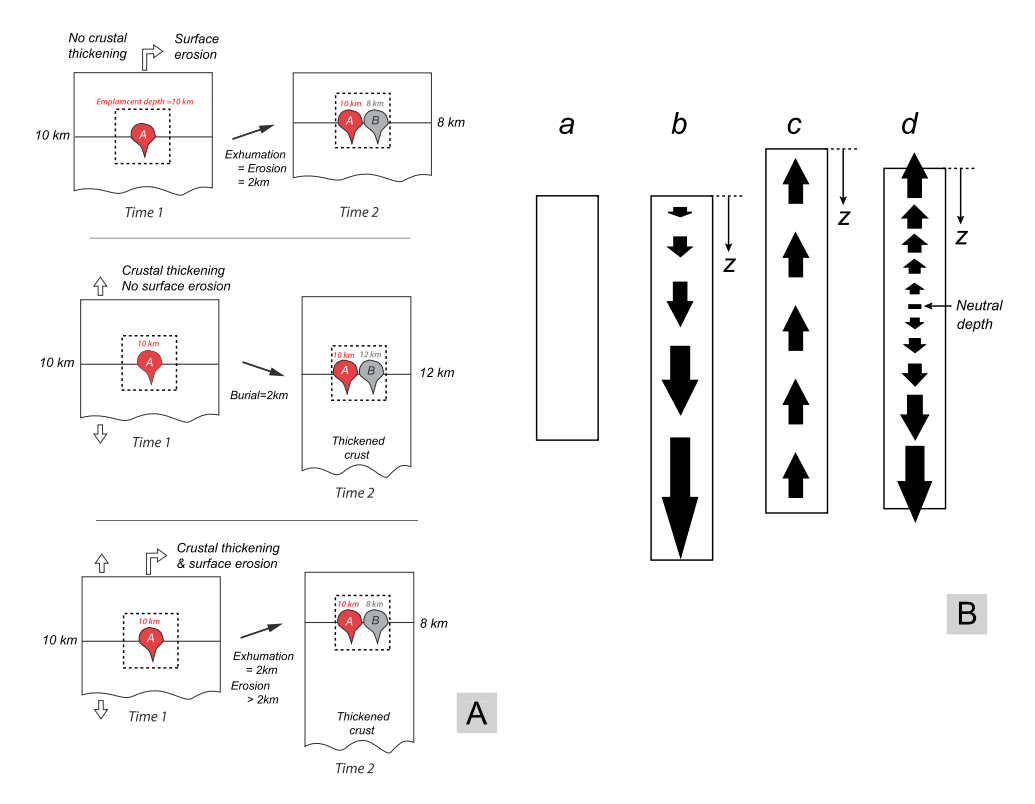


Fig. 6. (A) Exhumation or burial processes of block of crust (dashed box) tracked by emplacement depth (labeled on top of plutons) of two adjacent plutons. Top panel: only surface erosion, no crustal thickening. Emplacement depth difference equals exhumation and surface erosion. Middle panel: only crustal thickening, no surface erosion. Emplacement depth difference equals thickening-induced burial. Bottom panel: simultaneous crustal thickening and surface erosion. Emplacement depth difference equals exhumation but does not equal to erosion based on Eq. (1). (B) Kinematics of material transport within the crust. Arrows indicate the direction and relative magnitude (arrow length) of the vertical motion of the parcels of the rocks with respect to the surface. (a) Crust prior to deformation. (b) Homogenous thickening in crust. (c) Crust is subject to surface erosion. (d) Crust is subject to simultaneous crustal thickening and surface erosion. Neutral depth is the depth where the thickening-induced burial is balanced with surface erosion. z is the depth direction pointing downwards. Origin of z-axis is at the surface. Modified from Stüwe and Barr (1998).

we used here is quartz + plagioclase + K-feldspar + biotite + hornblende + magnetite + titanite or ilmenite + melt (assume originally present) corresponding to a system consisting of SiO₂-Al₂O₃-TiO₂-Fe₂O₃-FeO-MgO-CaO-Na₂O-K₂O. Using this mineral assemblage, we filtered out samples that did not meet the criterion. Petrographic descriptions and photomicrographs from each sample are presented in the Supplementary Materials.

We used two different calibrations to calculate the emplacement pressure: (1) the classic temperature-corrected calibration using plagioclase thermometry (Anderson and Smith, 1995; Holland and Blundy, 1994), and (2) a recent calibration that is better for low-P samples (Mutch et al., 2016). Independent constraints for pluton emplacement pressures include the appearance of magmatic epidote in plutons of medium-high emplacement pressures (Zen and Hammarstrom, 1984, Table 1) and the regional increase of metamorphic grade in the host rocks (Fig. 4).

Electron probe microanalysis (EPMA) was carried out at the Department of Earth, Environmental and Planetary Sciences at Rice University. To obtain the temperature of the solidus using the plagioclase thermometer (Holland and Blundy, 1994), we targeted five pairs of coexisting hornblende and plagioclase in each sample. At each pair, major element compositions of plagioclase and hornblende were made at 10 adjacent points (5 on hornblende, 5 on plagioclase). Inclusions, cracks, and retrograde rims were avoided. Hornblende and plagioclase formulas were then calculated based on 23 oxygens and 5 cations, respectively. Pressure and temperature were solved together using the Excel spreadsheet prepared by J.L. Anderson. Technical details of the EPMA analysis and pressure calculation spreadsheet are presented in the Supplementary Materials.

5.2. U/Pb zircon geochronology

Samples of plutons were processed for zircon separates following standard techniques involving crushing, magnetic separation, and heavy liquids. U-Pb geochronology of zircons was conducted by laser ablation inductively coupled plasma mass spectrometry (LA-ICP-MS) at the Arizona LaserChron Center. Cathodoluminescene (CL) images were used as a guide to avoid inclusions and cracks. Data reduction was performed with an in-house routine. We used TuffZirc algorithm in ISOPLOT to calculate the ages of plutonic samples. TuffZirc algorithm yields a more reliable igneous age by excluding ages of older xenocrysts or cores via a statically robust method rather than subjective decision (Ludwig and Mundil, 2002). Technical details of the LA-ICP-MS analysis are presented in the Supplementary Materials.

6. Results

6.1. Results of Al-in-hornblende barometry

Table 1 summarizes the 18 new pluton-emplacement pressures from the Al-in-Hbl barometry and solidus-temperatures derived from the plagioclase thermometry. Pressures show a variation from \sim 1 kbar to 8 kbar among samples and solidus temperatures show a range of 629-797 °C. When applying Anderson and Smith (1995)'s barometry, we found that in 12 out 18 samples, the hornblende compositions have either Fe³+/(Fe²+ + Fe³+) < 0.2 or Fe[#] < 0.4 that are not fully in the recommended ranges. For those samples, we present the pressures in parentheses. These pressures are still considered to be valid since the samples pass the Fe[#] < 0.65 and T < 800 °C filters suggested by Putirka (2016).

Pressures from Mutch et al. (2016)'s barometry were calculated for all samples. Mutch et al. (2016)'s calibration is not sensitive to temperature as long as the solidus is close to $725 \pm 75\,^{\circ}\mathrm{C}$ (Mutch et al., 2016). The calibration uncertainty of Anderson and Smith (1995)'s barometry is ± 0.6 kbar and the relative uncertainty of Mutch et al. (2016)'s barometry is 16%. Since these uncertainties obtained via barometry calibration cannot be used for natural samples, we assumed a standard error of 1 kbar to all samples instead. Within the uncertainties, pressures from Anderson and Smith (1995)'s and Mutch et al. (2016)'s calibrations overlap each other validating the results (Fig. S1). The final pressure of each sample is calculated using the mean value of the two calibrations. The depth of pluton emplacement is calculated using a characteristic crustal density of 2800 kg/m³. Full EPMA analytical data tables are presented in the Supplementary Materials.

6.2. Results of geochronology

Newly obtained U-Pb zircon ages from seven granitoid samples are reported in Table 1. Sample 7-6-1 is dated to 50.5 \pm 0.7 Ma (weighted mean age, 95% confidence, same for the rest samples) based on a coherent age group of 29 zircons. Sample XCT55 is dated to 177.5 \pm 1.1 Ma based on 29 zircons. Sample XCT56 is dated to 196.1 \pm 1.2 Ma based on 17 zircons. Sample XCT58 is dated to 46.4 \pm 0.4 Ma based on 19 zircons. Sample 10-8 is dated to 91.2 \pm 0.5 Ma based on 30 zircons. Sample 11-10 is dated to 63.8 \pm 0.5 Ma based on 27 zircons. Sample 12-14 is dated to 45.4 \pm 0.4 Ma based on 32 zircons. Full ICPMS analytical data tables and TuffZirc age plots are presented in the Supplementary Materials.

7. Discussion

7.1. Tilted crustal section of Gangdese Batholith

Fig. 4B and 4C shows the bedrock pressure data across the Gangdese Batholith from 90°E to 96°E. Near Lhasa (90.5°E to 92°E, Lhasa and Zedong sectors), the pressures have a relatively narrow range of 1 to 3 kbar. These pressures are consistent with the non-metamorphosed or greenschist-facies supracrustal rocks found in that area (Fig. 4A). To the east, pressure gradually increases from ~ 3 kbar to ~ 11 kbar between 92.5°E to 93.5°E (Jiacha and Wolong sectors). Pressures at the Nyingchi sector (~ 94.5 °E), where granulite-facies rocks are exposed (Zhang et al., 2010), are typically > 10 kbar with the highest pressure reaching 12.3 kbar. Further east of the Nyingchi (94.5°E to 96°E), pressures gradually shallow to 2.8 kbar except a metamorphic rock of 10.8 kbar exists at 95.2°E (Booth et al., 2009). At some places, juxtaposition of rocks of different paleo-depths and ages suggest significant vertical motion has occurred (see Section 7.3.2 for detailed discussion).

Longitudinal variations of pressure estimate and metamorphic grade show that the Gangdese bedrock pressure overall increases from west ($\sim 90^{\circ} E$) to east ($\sim 94.5^{\circ} E$). We interpret that the Gangdese Batholith was broadly tilted westward across from the Lhasa to Nyingchi sectors. To the east of Nyingchi, the crust was tilted eastward around the EHS.

The establishment of the paleo-depth of the Gangdese Batholith allows us to further address two topics. First, we can couple depth and age data to track the exhumation/burial paths. This addresses the juxtaposition of rocks of different paleo-depths. Second, we can constrain the differential exhumation that occurred along the orogen-parallel direction, which eventually results in the first-order longitude-pressure pattern observed at the surface today.

7.2. Kinematic model for exhumation during thickening and erosion

Here we present a one-dimensional kinematic model linking exhumation and burial processes in an orogen subject to simultaneous crustal thickening and surface erosion. This model provides insights to explain the first-order exhumation/burial pattern for the Gangdese Batholith discussed in Section 7.3. Fig. 6B illustrates the kinematics of a crustal column undergoing thickening or surface erosion (z-axis is positive downward, origin at surface). If we assume the thickening strain rate $\dot{\varepsilon}_z$ is homogenous across depth, the exhumation or burial of a parcel of rock at time t depends on the competition between thickening-induced burial ($\dot{\varepsilon}_z \cdot z$) and surface erosion (E) (Eq. (1)) (Stüwe and Barr, 1998).

$$v_e(t) = \frac{dz}{dt} = \dot{\varepsilon}_z \cdot z(t) - E \tag{1}$$

where v_e is the exhumation rate ($v_e < 0$) or burial rate ($v_e > 0$) such that if $v_e = 0$ the rock remains at the same depth ("neutral depth", Fig. 6B), E is the surface erosion rate, and z(t) is the depth of the parcel of the rock relative to the surface at time t. In order to obtain the exhumation/burial paths through time, we integrated the above equation assuming the surface erosion rate is a constant:

$$z(t) = \left(z_0 - \frac{E}{\dot{\varepsilon}_z}\right) \cdot e^{\dot{\varepsilon}_z t} + \frac{E}{\dot{\varepsilon}_z}$$
 (2)

where z_0 is the initial depth of the rock at time $t_0 = 0$. We understand that surface erosion rate can vary through time controlled by topography and climate parameters. The thickening strain rate could also be time- and depth-dependent in an orogen. The model is kept simple so as to show the relative roles of surface erosion and thickening-induced burial. Fig. 7 shows the exhumation/burial paths of parcels of rocks at 10, 20, and 40 km initial depths under different combinations of surface erosion rate and thickening strain rate. When E=0, all rocks experience burial; faster thickening strain rate results in faster burial (Fig. 7 A1-A3). Increased erosion rates can result in slower burial, or exhumation (e.g., Fig. 7 B1, C1, D1). We note that for some combinations of the $\dot{\varepsilon}_7$ and E_7 the exhumation path for rock at $z_0 = 10$ km remains effectively flat, suggesting the thickening-induced burial at 10 km depth is balanced by the surface erosion, resulting in minimal exhumation (Fig. 7 B1, C2, D3, highlighted by gray boxes). We obtain the following insights from this model:

- (1) The upper, middle, and lower crust exhume differently under same surface erosion and tectonic thickening conditions. This is because the thickening-induced burial rate $(\dot{\varepsilon_z} \cdot z)$ increases toward depth.
- (2) Rock can remain at a constant depth (neutral depth) if the thickening-induced burial balances erosion.
- (3) A tradeoff exists between erosion rate and thickening strain rate if we only know the exhumation/burial path at a given depth. A unique combination of erosion rate and thickening strain rate can be constrained if we know exhumation/burial paths of rocks at two different depths.

7.3. Exhumation history of Gangdese Batholith based on bedrock pressures

7.3.1. Justification of using bedrock pressures based on Gangdese geology

To track the exhumation history, we binned the bedrock pressures from the Lhasa-Nyingchi transect into five 50-100 km-sized sectors. From west to east, they are Lhasa sector, Zedong sector, Jiacha sector, Wolong sector, and Nyingchi sector (Fig. 2). Bedrock

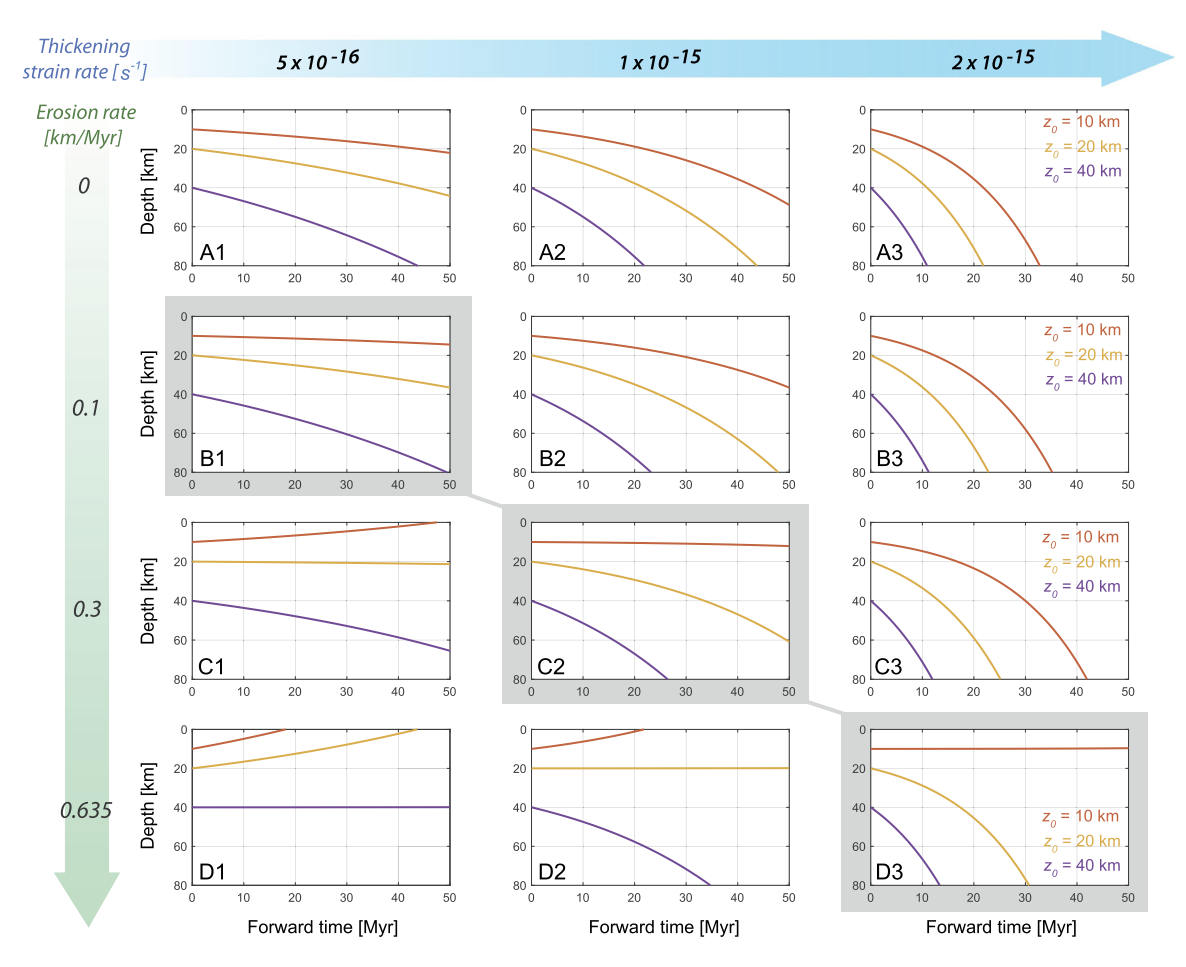


Fig. 7. Simulated exhumation-burial paths of rocks with different initial depths using Eq. (2). Surface erosion rate and thickening strain rate are varied. Three boxes are highlighted with gray color showing more or less flat exhumation paths for rocks at an initial depth of 10 km.

pressures to the east of Nyingchi are not binned because their pressure-associated ages are not well constrained. As previously mentioned, the assumption of using bedrock pressures to track exhumation is that no younger event affects the existing relative position between plutons or metamorphic host rocks. We further justify this assumption based on the geology in the study area. First, within each sector, younger shear zones of various dip directions and kinematics are required to juxtapose plutons or metamorphic host rocks of different depths and ages. In reality, only a few north-dipping, south-vergent orogen-parallel thrust faults have been recognized in the Lhasa-Nyingchi section of the Gangdese Batholith (Gangdese thrust, e.g., Yin et al., 1994). Near Zedong, where the 30-20 Ma Gangdese thrust has been mapped (Yin et al., 1994), our pressure data are all located in the upper plate of the thrust faults except one (1.8 kbar, 62 Ma) is located at the lower plate of an inferred fault trace. Even if we exclude this datapoint, the overall exhumation history is unaffected. Second, our pressure data are distributed parallel to the orogen with little room to develop complex orogen-parallel faults in between.

Two young (\sim 8-10 Ma) north-south trending normal faults are near or within the study area: the Nyainqentanglha and Cuona-Woka (Cona-Oiga) faults (Fig. 2). The \sim 8 Ma Nyainqentanglha fault located to the NW of Lhasa is a SE-dipping normal fault with a vertical throw of 12-15 km (Kapp et al., 2005). All of our pressure data are >70 km southeast of this fault, and more importantly, they are all located on its hanging wall side. Thus, we argue any tectonic exhumation related to the Nyainqentanglha fault does not affect the existing pressure pattern in the study area. The \sim 10 Ma Cuona-Woka faults located at \sim 92.3°E form a \sim 10-km-wide rift zone with two bounding normal faults dipping at \sim 60° (Wu et al.,

2008). The vertical throw of the Cuona-Woka faults is poorly documented. Since our data are all outside the rift zone, the Cuona-Woka rift is unlikely to affect the regional pressure pattern in the study area.

7.3.2. The exhumation/burial paths of Gangdese crust

The exhumation/burial paths of the five sectors is shown in Fig. 3C. Since different longitudinal sectors represent rocks of different paleo-depths, these paths reveal contrasting exhumation/burial histories for rocks of different crustal levels before the tilting occurred. The two west sectors (Lhasa and Zedong), representing the upper crust, show relatively flat paths suggesting the exhumation of the two sectors is limited (\sim 10 km) since Late Cretaceous. In contrast, the two eastern sectors (Wolong and Nyingchi), representing the middle-lower crust, show a complex pattern with multiple burial and exhumation trajectories. Only three samples were collected from the Jiacha sector; therefore its exhumation path is not clear based on the available data. Two pressures associated with Early Jurassic age (177.5 Ma and 196.1 Ma) are not discussed here since we focus on the Gangdese history since 100 Ma. To facilitate discussion, we divide the exhumation history into 4 stages based on the pattern of the exhumation paths and regional geological history.

Stage 1 (100-70 Ma) represents the Late Cretaceous phase of the Gangdese continental arc (Fig. 3E). Samples from the Lhasa sector remain isobaric at 2 kbar (\sim 7-8 km depth) during this stage. In contrast, the Wolong sector shows progressive burial from 20 km to 40 km from ca. 95 Ma to 72 Ma. The average burial rate is about 1 km/Myr (Fig. 3C). Our available data cannot recover its temporal pattern of the deeper Nyingchi sector during this stage,

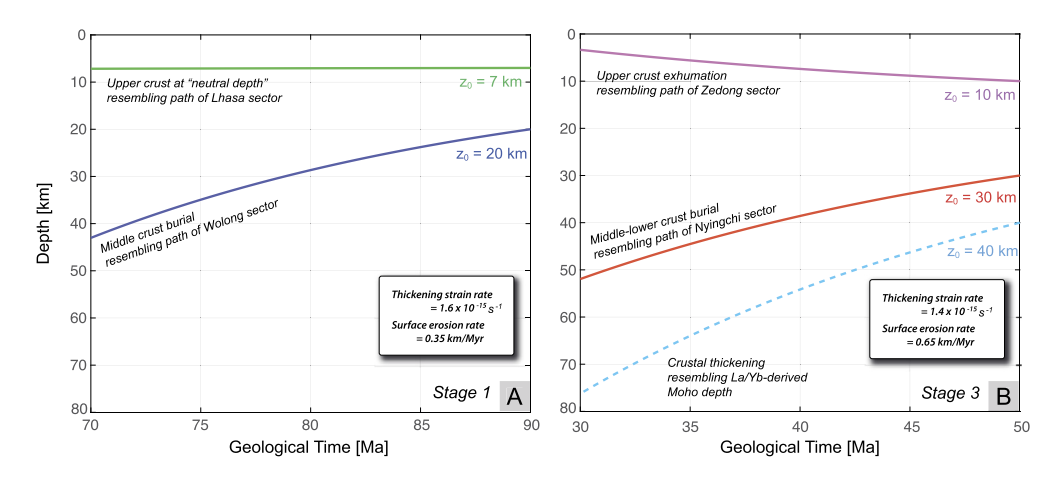


Fig. 8. (A) Simulated exhumation-burial paths for parcels of rocks at 7 km and 20 km under a thickening strain rate of 1.6×10^{-15} s⁻¹ and a surface erosion rate of 0.35 km/Myr. These simulated paths resemble the exhumation-burial paths constrained by the bedrock pressures in the Lhasa and Wolong sectors during Stage 1. (B) Simulated exhumation-burial paths for parcels of rocks at 10 km and 30 km and Moho depth at 40 km under a thickening strain rate of 1.4×10^{-15} s⁻¹ and a surface erosion rate of 0.65 km/Myr. These simulated paths resemble the exhumation-burial paths constrained by the bedrock pressures in the Zedong and Niyingchi sectors and the $(La/Yb)_n$ -derived crustal thickness during Stage 3. Crustal thickness of 40 km is used at 50 Ma.

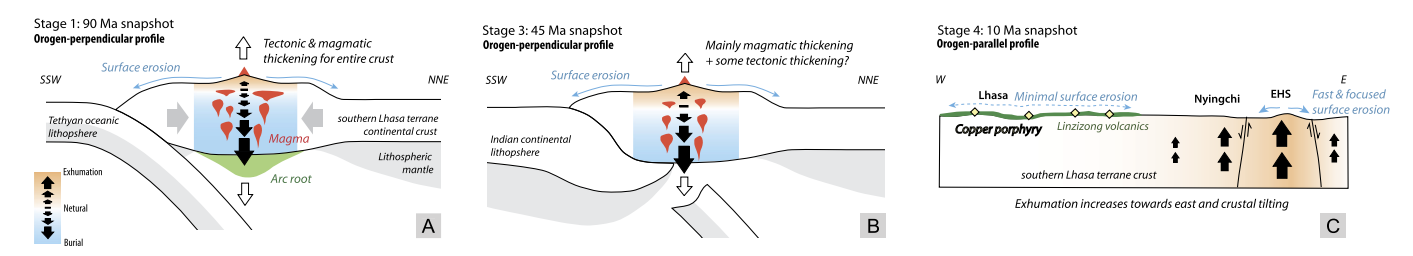


Fig. 9. Cartoon of snapshots showing the tectonic evolution of the Gangdese Batholith highlighting the exhumation and burial processes in different depths of the crust. The color bar with arrowheads indicates the motion of rocks relative to the surface (exhumation, neutral or burial). (A) During Stage 1 at 90 Ma, the entire crust was thickened by magmatic inflation and tectonic thickening. Arc root is generated. (B) During Stage 3 at 45 Ma, the crust was mainly thickened by magmatic inflation and some tectonic thickening. (C) During Stage 4 at 10 Ma, the eastern part of the section experienced fast exhumation related to the focused surface erosion at the EHS. The western part of the section has minimal surface erosion and exhumation. Such differential exhumation causes the tilting of the crustal section. Note, (A), (B), are shown for orogen-perpendicular profile, and (C) is shown for orogen-parallel profile. EHS: Eastern Himalayan Syntaxis.

but it probably experienced burial similar to the Wolong sector given the spatial proximity.

The different exhumation-burial paths for the upper and middle crust resemble the simulated exhumation/burial paths shown in Fig. 8A in which a thickening strain rate of $1.6 \times 10^{-15} \, \mathrm{s}^{-1}$ and a surface erosion rate of $0.35 \, \mathrm{km/Myr}$ are applied. Several lines of evidence from other orogens support the proposed strain rate and erosion rate. For example, the thickening strain rate of the Mesozoic Sierra Nevada continental arc is estimated from $10^{-15} \, \mathrm{s}^{-1}$ to $10^{-16} \, \mathrm{s}^{-1}$ (Cao et al., 2015). An erosion rate of $0.35 \, \mathrm{km/Myr}$ is also reasonable for many magmatic orogens, such as the Cretaceous Peninsular Range Batholith, which is constrained to 0.2-1 km/Myr (Jiang and Lee, 2017). Mass balance-isostasy modeling for the Cretaceous central Sierra Nevada suggests a 0.2- $0.5 \, \mathrm{km/Myr}$ surface erosion rate (Cao and Paterson, 2016).

In Late Cretaceous (100-70 Ma), the Gangdese crust experienced thickening as predicted by the simple kinematic model (Fig. 8A; Fig. 9A). The Gangdese arc experienced a magmatic flare-up at 100-90 Ma (Chapman and Kapp, 2017) (Fig. 3A) and a major phase of Late Cretaceous (100-70 Ma) north-south shortening (Fig. 3E) (Kapp et al., 2007). Accordingly, magmatic inflation and contractional deformation probably contributed to the inferred thickening. Similar combined tectonic-magmatic thickening has been proposed for North and South American Cordillera (e.g., Allmendinger et al., 1997; Cao et al., 2015), as well as the Gangdese arc (Zhu et al., 2017; DePaolo et al., 2019). However, the relative contributions of magmatic versus tectonic thickening are unknown.

Stage 2 (70-50 Ma) represents a transition phase from continental arc to continental collision that occurred around 55-60 Ma

(e.g., DeCelles et al., 2014, Fig. 3E). For the upper crust, the exhumation paths of the Lhasa and Zedong Sectors remains relatively flat (Fig. 3C).

A second magmatic flare-up peaked at ca. 55 Ma, and evidence for major tectonic deformation in the study area is lacking during this period except a brief shortening event in the retro-arc (Kapp et al., 2007, Fig. 3E). For the upper crust, the relative flat exhumation path may suggest that the surface erosion was still more or less balanced by the magmatic thickening and the deposition of the Linzizong volcanics.

Although the number of data points for Stage 2 are insufficient to make meaningful interpretations for middle-lower crust, several dynamic processes may compete with one another during this transition period and complicate the behavior of the middle-lower crust. Proposed processes include arc-root founding at 69-50 Ma (Kapp et al., 2007), slab breakoff and subsequent upwelling of the asthenospheric mantle at 53 Ma (Zhu et al., 2015), or Gangdese lithosphere delamination at 68-60 Ma (Ji et al., 2014). More data is needed to constrain the behavior of the middle-lower crust.

Stage 3 (50-30 Ma) represents the early phase of continental collision. The upper crust exhumation path of the Zedong sector slightly goes up from 10 km to \sim 3 km corresponding to an average exhumation rate of 0.35 km/Myr. For the middle-lower crust, the Nyingchi sector experienced burial from 30 km to \sim 45 km, corresponding to an average burial rate of 0.75 km/Myr (Fig. 3C). Referring to our kinematic model, we find that when the thickening strain rate is $1.4 \times 10^{-15} \ \rm s^{-1}$, and surface erosion rate is 0.65 km/Myr, the simulated exhumation/burial paths for 10 km

and 30 km deep rocks mimic the exhumation/burial paths in Stage 3 (Fig. 8B).

Crustal thickening during this stage was mainly caused by magmatic inflation during the later stage of the second flare-up (50-60 Ma) and possibly some syn-collisional shortening starting at $\sim\!42$ Ma evidenced by the accelerated cooling in the retro-arc Linzhou area (He et al., 2007) (Fig. 3E; Fig. 9B). Using La/Yb ratios from the Gangdese plutons to track the crustal thickness, Zhu et al. (2017) shows that the crust thickened between 50 and 30 Ma (Fig. 3D). DePaolo et al. (2019) also suggested major crustal thickening (>30 km thickening) took place between 45 and 32 Ma to the north of the suture near Lhasa based on Nd isotopes and La/Yb data.

The middle-lower crust has thus experienced two burial processes, one in Late Cretaceous related to the continental arc, and the other one in Eocene related to the collision (Fig. 3C). Such burial processes have been recognized by two-stage granulite facies metamorphism by Zhang et al. (2010) in the high-grade terrane near Nyingchi. The collision-related burial is also shown by the P-T-t path of the high-grade rocks from Nyingchi area (Tian et al., 2020).

Stage 4 (30-0 Ma) represents a phase of continued collisional plate convergence and crustal tilting due to differential exhumation along the Lhasa-Nyingchi section (Fig. 3C, Fig. 9C). Although bedrock pressure data is not available during this stage, compiled low-temperature thermochronological data in Lhasa-Zedong area reveal a major cooling event from 25 to 10 Ma (Fig. 3B). Since the closure temperature of the zircon fission track system is ~250 °C (e.g., Reiners and Brandon, 2006), the amount of exhumation constrained by the low-temperature thermochronological data is about 6-8 km assuming a 40-30 °C /km geothermal gradient. This corresponds to an average exhumation of about 0.4-0.5 km/Myr during 25-10 Ma. If the cooling was more temporally concentrated within 16-12 Ma (Tremblay et al., 2015), the exhumation rate could have been greater at 1.5-2 km/Myr. After 10 Ma, surface erosion in the Lhasa and Zedong Sectors was minimal, <1 km (<0.1 km/Myr) (Tremblay et al., 2015). This interpretation is further supported by the preservation of 20-10 Ma copper porphyry deposits in Lhasa-Zedong area (Fig. 3C).

In contrast, the Nyingchi sector had to have exhumed from at least 45 km depth to the surface during this stage, which corresponds to an average exhumation rate of 1.5 km/Myr (Zeitler et al., 2014). The exact exhumation paths of the Nyingchi sectors are unknown. Given the spatial proximity of the Nyingchi sector to the Eastern Himalayan Syntaxis, we speculate that the Nyingchi sector exhumed together with the Eastern Himalayan Syntaxis since ca. 10 Ma (Ding et al., 2001) with an exhumation rates of \sim 5-10 km/Myr since ca. 10-5 Ma (e.g., Booth et al., 2009; Zeitler et al., 2014) (Fig. 3C).

During Stage 4, north-south contractional deformation resumed in the southern Lhasa terrane represented by the 27-23 Ma Gangdese Thrust and Late Oligocene-Early Miocene Great Counter Thrust (Yin and Harrison, 2000; Laskowski et al., 2018, Fig. 3E). This phase of contraction resulted in ∼20% shortening strain of the Linzizong volcanics during 30-10 Ma (Pan and Kidd, 1999). The activation of the Gangdese Thrust and Great Counter Thrust could be responsible for the coeval major cooling events (Laskowski et al., 2018). The shortening-related crustal thickening resulted in isostatic elevation increase near the Lhasa-Zedong area, but the elevation increase does not induce a fast erosion probably because the mountain building in the Himalaya region shifted the erosional front southwards after 10 Ma (Tremblay et al., 2015). In contrast to the minimal exhumation in the Lhasa and Zedong sectors, the fast exhumation of the Nyingchi sector is probably related to the fast and focused erosion-driven exhumation of the Eastern Himalayan Syntaxis (e.g. Zeitler et al., 2014). We suggest that crustal tilting from Lhasa-Nyingchi section occurred during this stage due to the

dramatic exhumation difference between the Lhasa and Nyingchi areas (Fig. 9C).

7.4. Comparison to La/Yb proxy for crustal thickness

Whole-rock Sr/Y and $(La/Yb)_n$ have been recently used as proxies for crustal thickness (e.g., Profeta et al., 2015). Zhu et al. (2017) used whole-rock $(La/Yb)_n$ from Gangdese plutons to track crustal thickness in the southern margin of the Lhasa terrane. To compare their results to the bedrock pressures in the study area, we filtered Zhu et al. (2017) data using the spatial range of the study area (90-95°E, 29-30°N) (Fig. 3D).

For Stage 1, most of the $(La/Yb)_n$ data cannot be used to track crustal thickness since the plutons are likely originated from the oceanic slab melts (Zhu et al., 2017). Thus, the comparison between the $(La/Yb)_n$ -derived crustal thickness and the burial paths from the bedrock pressures cannot be made.

For Stage 2, the crustal thickness derived from $(\text{La/Yb})_n$ shows a scattered distribution while the bedrock pressure data are too limited to make robust interpretations.

For Stage 3, the $(\text{La/Yb})_n$ -derived crustal thickness increased from 30-50 km to $\sim\!80$ km, consistent with the burial path of the Niyingchi sector. If we assume the crustal thickness was 40 km at 50 Ma, with the proposed thickening strain rate $(1.4\times10^{-15}~\text{s}^{-1})$ and surface erosion rate (0.65~km/Myr), the crustal thickness could achieve $\sim\!80~\text{km}$ by 30 Ma (Fig. 8B).

For Stage 4, the $(La/Yb)_n$ -derived crustal thickness shows a similar value to the present-day thickness (\sim 70 km). The bedrock pressure does not cover this stage. Since the EHS has been exhumed for >40 km since \sim 10 Ma (Zeitler et al., 2014), it may require a lower crustal flow to compensate the exhumation/thinning of the EHS crust and its vicinity (e.g., Zeitler et al., 2014).

In summary, we argue that the bedrock pressure is supplementary to the $(\text{La/Yb})_n$ -derived crustal thickness, and they can be used together to test tectonic models. Two datasets are consistent with each other during the early phase of continental collision (50-30 Ma). For other stages, due to the incompleteness of datasets, either $(\text{La/Yb})_n$ or bedrock pressure, the comparison cannot be fully made. More studies are needed to fill the gaps.

7.5. Outstanding questions

Bedrock pressure samples were mostly obtained along the Indus-Yarlung suture in this study, and an E-W bedrock pressure gradient is revealed. What is the regional pattern of bedrock pressures outside the study area, especially further towards the west and in the suture-perpendicular direction? Is the batholith also tilted in the N-S direction due to the Oligocene-Miocene structures that are localized in the southern part of the batholith (e.g., the Great Counter Thrust and Gangdese Thrust)? Do other segments of the Gangdese Batholith also show the same two phases of burial related to the continental arc and continental collision? More bedrock pressures are needed to answer these questions. Eventually, with enough data, once can produce a bedrock pressure map of high spatial resolution similar to the one for the Sierra Nevada Batholith (e.g., Chapman et al., 2012). Such regional pressure patterns can be further coupled with the geochronology, geochemistry, isotopes, and magmatic fabrics to investigate depthdependent processes associated with the arc magmatism and continental collision (e.g., Jagoutz, 2014).

The tilting mechanisms of the Batholith are not discussed in this study. Several possible end-members could be (1) rigid-body-like tilting across a large (~400 km) area, (2) tilting accommodated by multiple orogen-perpendicular shear zones, and (3) along-strike crustal flow related to the exhumation of the EHS. Are there unmapped orogen-perpendicular shear zones in the study area per-

mitting east-side-up kinematics? How does the mechanical coupling between the fast-exhuming EHS and the Gangdese crust affect the degree of the tilting? Field studies should be combined with 2D and 3D geodynamic modeling to answer these questions.

Finally, what is the CO_2 consumption related to the erosion and the silicate weathering of the Gangdese Batholith, especially during the continental arc stage and during the last ~ 10 Myr when the batholith was tilted? For example, one could estimate the amount of crustal materials eroded from the Gangdese Batholith since 10 Ma by integrating the area above the bedrock pressures (Fig. 4B). Such estimates can provide a basis to investigate the roles of magmatic orogens in the long-term carbon budget by evaluating the CO_2 outgassing versus the CO_2 consumption through erosion-chemical weathering processes (Jiang and Lee, 2019).

8. Conclusions

Longitudinal bedrock pressure pattern has been revealed in the Gangdese Batholith from Lhasa to Nyingchi. Bedrock pressure increase from 1-2 kbar near Lhasa to 6-12 kbar near Nyingchi. Upper and middle-lower crust rocks experienced differential exhumation or burial processes since Late Cretaceous. Dramatic differential exhumation along the E-W direction occurred since ca. 10 Ma, which tilted the crust to the present-day exposure levels. The exhumation-burial history of the Gangdese Batholith reflects integrated tectonic, magmatic, and surface processes.

Declaration of competing interest

The authors declare that they have no known competing financial interests or personal relationships that could have appeared to influence the work reported in this paper.

Acknowledgements

This study is supported by the National Natural Science Foundation of China (41888101), the second Tibetan Plateau Scientific Expedition and Research Program (STEP) Grant (2019OZKK0802). National Science Foundation (NSF) grants (EAR-1830139: EAR-1914501), and Chinese Academy of Sciences State Key Laboratory of Lithospheric Evolution grant (SKL-Z201706). NSF grant EAR-1649254 is acknowledged for the support of the Arizona Laser-Chron Center. We thank Gelu Costin at Rice EPMA lab for helping with the analysis, UNR undergraduate student Anthony Florez for map digitalization using QGIS, and Hao Zhang, Ming Tang for field assistance. John McCormack is thanked for the help with mineral identification. We appreciate conversations and feedback at the NSF-supported (EAR-1912713) Himalayan-Karakoram-Tibet 2019 meeting in Bozeman, MT. We thank Paul Kapp, Andrew K. Laskowski, Keith Putirka, and an anonymous reviewer for their critical comments helped to improve the quality of the manuscript. Editor An Yin is thanked for handling the manuscript.

Appendix A. Supplementary material

Supplementary material related to this article can be found online at https://doi.org/10.1016/j.epsl.2020.116347.

References

- Ague, J.J., Brandon, M.T., 1992. Tilt and northward offset of Cordilleran batholiths resolved using igneous barometry. Nature 360, 146–149. https://doi.org/10.1038/360146a0.
- Allmendinger, R.W., Jordan, T.E., Kay, S.M., Isacks, B.L., 1997. The evolution of the Altiplano-Puna plateau of the Central Andes. Annu. Rev. Earth Planet. Sci. 25 (1), 139–174.
- Anderson, J.L., Smith, D.R., 1995. The effects of temperature and fO₂ on the Al-in-hornblende barometer. Am. Mineral. 80 (5-6), 549-559.

- Booth, A.L., Chamberlain, C.P., Kidd, W.S.F., Zeitler, P.K., 2009. Constraints on the metamorphic evolution of the eastern Himalayan syntaxis from geochronologic and petrologic studies of Namche Barwa. Geol. Soc. Am. Bull. 121, 385–407. https://doi.org/10.1130/B26041.1.
- Cao, W., Paterson, S., 2016. A mass balance and isostasy model: exploring the interplay between magmatism, deformation, and surface erosion in continental arcs using central Sierra Nevada as a case study. Geochem. Geophys. Geosyst., 1–19. https://doi.org/10.1002/2015GC006229.
- Cao, W., Paterson, S., Memeti, V., Mundil, R., Anderson, J.L., Schmidt, K., 2015. Tracking paleodeformation fields in the Mesozoic central Sierra Nevada arc: implications for intra-arc cyclic deformation and arc tempos. Lithosphere 7, 296–320. https://doi.org/10.1130/L389.1.
- Chapman, A.D., Saleeby, J.B., Wood, D.J., Piasecki, A., Kidder, S., Ducea, M.N., Farley, K.A., 2012. Late Cretaceous gravitational collapse of the southern Sierra Nevada batholith, California. Geosphere 8 (2), 314–341.
- Chapman, J.B., Kapp, P., 2017. Tibetan magmatism database. Geochem. Geophys. Geosyst. 18 (11), 4229–4234.
- Chung, S.-L., Chu, M.-F., Ji, J., O'Reilly, S.Y., Pearson, N.J., Liu, D., Lee, T.-Y., Lo, C.-H., 2009. The nature and timing of crustal thickening in Southern Tibet: geochemical and zircon Hf isotopic constraints from postcollisional adakites. Tectonophysics 477, 36–48. https://doi.org/10.1016/j.tecto.2009.08.008.
- Dai, J., Wang, C., Hourigan, J., Li, Z., Zhuang, G., 2013. Exhumation history of the Gangdese Batholith, southern Tibetan plateau: evidence from apatite and zircon (U-Th)/He thermochronology. J. Geol. 121, 155–172. https://doi.org/10.1086/ 669250
- DeCelles, P.G., Kapp, P., Quade, J., Gehrels, G.E., 2011. Oligocene-miocene Kailas basin, southwestern Tibet: record of postcollisional upper-plate extension in the Indus-Yarlung suture zone. Geol. Soc. Am. Bull. 123, 1337–1362. https://doi.org/10.1130/B30258.1.
- DeCelles, P.G., Kapp, P., Gehrels, G.E., Ding, L., 2014. Paleocene-Eocene foreland basin evolution in the Himalaya of southern Tibet and Nepal: implications for the age of initial India-Asia collision. Tectonics 33 (5), 824–849.
- DePaolo, D.J., Harrison, T.M., Wielicki, M., Zhao, Z., Zhu, D.-C., Zhang, H., Mo, X., 2019. Geochemical evidence for thin syn-collision crust and major crustal thickening between 45 and 32 Ma at the southern margin of Tibet. Gondwana Res., 1–57. https://doi.org/10.1016/j.gr.2019.03.011.
- Ding, L., Zhong, D., Yin, A., Kapp, P., Harrison, T.M., 2001. Cenozoic structural and metamorphic evolution of the eastern Himalayan syntaxis (Namche Barwa). Earth Planet. Sci. Lett. 192 (3), 423–438.
- Ducea, M.N., Saleeby, J.B., Bergantz, G., 2015. The architecture, chemistry, and evolution of continental magmatic arcs. Annu. Rev. Earth Planet. Sci. 43, 299–331. https://doi.org/10.1146/annurev-earth-060614-105049.
- Hammarstrom, J.M., Zen, E.A., 1986. Aluminum in hornblende: an empirical igneous geobarometer. Am. Mineral. 71 (11–12), 1297–1313.
- Harrison, T.M., Yin, A., Grove, M., Lovera, O.M., Ryerson, F.J., Zhou, X., 2000. The Zedong Window: a record of superposed Tertiary convergence in southeastern Tibet. J. Geophys. Res., Solid Earth 105, 19211–19230. https://doi.org/10.1029/ 20001B900078.
- He, S., Kapp, P., DeCelles, P.G., Gehrels, G.E., Heizler, M., 2007. Cretaceous–Tertiary geology of the Gangdese arc in the Linzhou area, southern Tibet. Tectonophysics 433 (1–4), 15–37.
- Holland, T., Blundy, J., 1994. Non-ideal interactions in calcic amphiboles and their bearing on amphibole-plagioclase thermometry. Contrib. Mineral. Petrol. 116, 433–447. https://doi.org/10.1007/BF00310910.
- Jagoutz, O., 2014. Arc crustal differentiation mechanisms. Earth Planet. Sci. Lett. 396, 267–277. https://doi.org/10.1016/j.epsl.2014.03.060.
- Ji, W.Q., Wu, F.Y., Chung, S.L., Li, J.X., Liu, C.Z., 2009. Zircon U-Pb geochronology and Hf isotopic constraints on petrogenesis of the Gangdese batholith, southern Tibet. Chem. Geol. 262 (3-4), 229-245.
- Ji, W.Q., Wu, F.Y., Liu, C.Z., Chung, S.L., 2012. Early Eocene crustal thickening in southern Tibet: New age and geochemical constraints from the Gangdese batholith. J. Asian Earth Sci. 53, 82–95.
- Ji, W.-Q., Wu, F.-Y., Chung, S.-L., Liu, C.-Z., 2014. The Gangdese magmatic constraints on a latest Cretaceous lithospheric delamination of the Lhasa terrane, southern Tibet. Lithos 210–211, 1–13. https://doi.org/10.1016/j.lithos.2014.10.001.
- Jiang, H., Lee, C.-T.A., 2017. Coupled magmatism-erosion in continental arcs: reconstructing the history of the Cretaceous Peninsular Ranges batholith, southern California through detrital hornblende barometry in forearc sediments. Earth Planet. Sci. Lett. 472, 69–81. https://doi.org/10.1016/j.epsl.2017.05.009.
- Jiang, H., Lee, C.-T.A., 2019. On the role of chemical weathering of continental arcs in long-term climate regulation: a case study of the Peninsular Ranges batholith, California (USA). Earth Planet. Sci. Lett. 525, 115733.
- Jiang, Z.Q., Wang, Q., Wyman, D.A., Li, Z.X., Yang, J.H., Shi, X.B., Ma, L., Tang, G.J., Gou, G.N., Jia, X.H., Guo, H.F., 2014. Transition from oceanic to continental lithosphere subduction in southern Tibet: Evidence from the Late Cretaceous–Early Oligocene (91–30 Ma) intrusive rocks in the Chanang–Zedong area, southern Gangdese. Lithos 196, 213–231.
- Kapp, J.L.D., Harrison, T.M., Kapp, P., Grove, M., Lovera, O.M., Lin, D., 2005. Nyain-qentanglha Shan: a window into the tectonic, thermal, and geochemical evolution of the Lhasa block, southern Tibet. J. Geophys. Res. 110, B08413. https://doi.org/10.1029/2004JB003330.

- Kapp, P., DeCelles, P.G., Leier, A.L., Fabijanic, J.M., He, S., Pullen, A., Gehrels, G.E., Ding, L., 2007. The Gangdese retroarc thrust belt revealed. GSA Today 17 (7), 4.
- Laske, G., Masters, G., Ma, Z., Pasyanos, M., 2013. April. Update on CRUST1.0—A 1-degree global model of Earth's crust. Geophys. Res. Abstr, vol. 15. EGU General Assembly. Vienna. Austria. p. 2658.
- Laskowski, A.K., Kapp, P., Cai, F., 2018. Gangdese culmination model: oligocene-miocene duplexing along the India-Asia suture zone, Lazi region, southern Tibet. Geol. Soc. Am. Bull. 130, 1355–1376. https://doi.org/10.1130/B31834.1.
- Lee, C.T.A., Shen, B., Slotnick, B.S., Liao, K., Dickens, G.R., Yokoyama, Y., Lenardic, A., Dasgupta, R., Jellinek, M., Lackey, J.S., Schneider, T., 2013. Continental arc-island arc fluctuations, growth of crustal carbonates, and long-term climate change. Geosphere 9 (1), 21–36.
- Ludwig, K.L., Mundil, R., 2002. Extracting reliable U-Pb ages and errors from complex populations of zircons from Phanerozoic tuffs. In: 12th Goldschmidt Conference. J. Conf. Abstr. A-463.
- Ma, L., Wang, Q., Wyman, D.A., Li, Z.X., Jiang, Z.Q., Yang, J.H., Gou, G.N., Guo, H.F., 2013. Late Cretaceous (100–89 Ma) magnesian charnockites with adaktitic affinities in the Milin area, eastern Gangdese: Partial melting of subducted oceanic crust and implications for crustal growth in southern Tibet. Lithos 175, 315–332.
- Mutch, E.J.F., Blundy, J.D., Tattitch, B.C., Cooper, F.J., Brooker, R.A., 2016. An experimental study of amphibole stability in low-pressure granitic magmas and a revised Al-in-hornblende geobarometer. Contrib. Mineral. Petrol. 171 (10), 85.
- Pan, Y., Kidd, W.S.F., 1999. Shortening in the southern Lhasa block during India-Asia collision. In: Abstract of 14th Himalaya-Karakoram-Tibet Workshop. Kloster Ettal. Germany.
- Profeta, L., Ducea, M.N., Chapman, J.B., Paterson, S.R., Gonzales, S.M.H., Kirsch, M., Petrescu, L., DeCelles, P.G., 2015. Quantifying crustal thickness over time in magmatic arcs. Sci. Rep. 5, 17786. https://doi.org/10.1038/srep17786.
- Putirka, K., 2016. Amphibole thermometers and barometers for igneous systems and some implications for eruption mechanisms of felsic magmas at arc volcanoes. Am. Mineral. 101, 841–858. https://doi.org/10.2138/am-2016-5506.
- Reiners, P.W., Brandon, M.T., 2006. Using thermochronology to understand orogenic erosion. Annu. Rev. Earth Planet. Sci. 34, 419–466.
- Stüwe, K., Barr, T.D., 1998. On uplift and exhumation during convergence. Tectonics 17, 80–88. https://doi.org/10.1029/97TC02557.
- Tian, Z., Brown, M., Zhang, Z., Piccoli, P.M., Dong, X., 2020. Contrasting CW and CCW tectono-metamorphic belts in the eastern Himalayan syntaxis: quantification of P-T-t paths and tectonic interpretation. Gondwana Res. 79, 1–26.
- Tremblay, M.M., Fox, M., Schmidt, J.L., Tripathy-Lang, A., Wielicki, M.M., Harrison, T.M., Zeitler, P.K., Shuster, D.L., 2015. Erosion in southern Tibet shut down at ∼10 Ma due to enhanced rock uplift within the Himalaya. Proc. Natl. Acad. Sci. 112, 12030–12035. https://doi.org/10.1073/pnas.1515652112.

- Willett, S.D., 1999. Orogeny and orography: the effects of erosion on the structure of mountain belts. J. Geophys. Res., Solid Earth 104 (B12), 28957–28981.
- Wu, Z.-H., Zhang, Y.-S., Hu, D.-G., Zhao, X.-T., Ye, P.-S., 2008. The quaternary normal faulting of the Cona-Oiga rift. Seismol. Geol. 30, 144–160. In Chinese with English abstract.
- Yang, Z.M., Goldfarb, R., Chang, Z.S., 2016. Generation of postcollisional porphyry copper deposits in southern Tibet triggered by subduction of the Indian continental plate. In: Society of Economic Geologists Special Publication, vol. 19, pp. 279–300.
- Yanites, B.J., Kesler, S.E., 2015. A climate signal in exhumation patterns revealed by porphyry copper deposits. Nat. Geosci. 8 (6), 462–465.
- Yin, A., Harrison, T.M., 2000. Geologic evolution of the Himalayan-Tibetan orogen. Annu. Rev. Earth Planet. Sci. 28 (1), 211–280.
- Yin, A., Harrison, T.M., Ryerson, F.J., Wenji, C., Kidd, W.S.F., Copeland, P., 1994. Tertiary structural evolution of the Gangdese Thrust System, southeastern Tibet. J. Geophys. Res., Solid Earth 99, 18175–18201. https://doi.org/10.1029/94/B00504.
- Yin, J., Xu, J., Liu, C., Li, H., 1988. The Tibetan plateau: regional stratigraphic context and previous work. Philos. Trans. R. Soc. Lond. Ser. A, Math. Phys. Sci. 327 (1594), 5–52.
- Zeitler, P.K., Meltzer, A.S., Brown, L., Kidd, W.S., Lim, C., Enkelmann, E., 2014. Tectonics and topographic evolution of Namche Barwa and the easternmost Lhasa block, Tibet. In: Toward an Improved Understanding of Uplift Mechanisms and the Elevation History of the Tibetan Plateau. In: Geological Society of America Special Paper, vol. 507, pp. 23–58.
- Zen, E.A., Hammarstrom, J.M., 1984. Magmatic epidote and its petrologic significance. Geology 12 (9), 515–518.
- Zhang, Z.M., Zhao, G.C., Santosh, M., Wang, J.L., Dong, X., Liou, J.G., 2010. Two stages of granulite facies metamorphism in the eastern Himalayan syntaxis, south Tibet: petrology, zircon geochronology and implications for the subduction of Neo-Tethys and the Indian continent beneath Asia. J. Metamorph. Geol. 28 (7), 719–733.
- Zhang, L.Y., Ducea, M.N., Ding, L., Pullen, A., Kapp, P., Hoffman, D., 2014. Southern Tibetan Oligocene–Miocene adakites: A record of Indian slab tearing. Lithos 210, 209–223.
- Zhu, D.-C., Wang, Q., Zhao, Z.-D., Chung, S.-L., Cawood, P.A., Niu, Y., Liu, S.A., Wu, F.-Y., Mo, X.-X., 2015. Magmatic record of India-Asia collision. Sci. Rep. 5, 14289.
- Zhu, D.-C., Wang, Q., Cawood, P.A., Zhao, Z.-D., Mo, X.-X., 2017. Raising the Gangdese Mountains in southern Tibet. J. Geophys. Res., Solid Earth 122, 214–223. https:// doi.org/10.1002/2016/B013508.
- Zuza, A.V., Wu, C., Wang, Z., Levy, D.A., Li, B., Xiong, X., Chen, X., 2018. Underthrusting and duplexing beneath the northern Tibetan Plateau and the evolution of the Himalayan-Tibetan orogen. Lithosphere 11 (2), 209–231.